Biogeosciences Discuss., https://doi.org/10.5194/bg-2017-554
Manuscript under review for journal Biogeosciences
Discussion started: 4 January 2018

Climate and marine biogeochemistry during the Holocene from transient model simulations

Joachim Segschneider[1], **Birgit Schneider**[1], and **Vyacheslav Khon**[1]

[1]Institute of Geosciences, Christian-Albrechts University of Kiel, Ludewig-Meyn-Str. 10,
D-24118 Kiel, Germany

Correspondence to: J. Segschneider (joachim.segschneider@ifg.uni-kiel.de)

Biogeosciences Discuss., https://doi.org/10.5194/bg-2017-554
Manuscript under review for journal Biogeosciences
Discussion started: 4 January 2018

Abstract

Climate and marine biogeochemistry changes over the Holocene are investigated based on transient global climate and biogeochemistry model simulations over the last 9,500 yr. The simulations are forced by accelerated and non-accelerated orbital parameters, respectively, and atmospheric pCO_2. The analysis focusses on key climatic parameters of relevance to the marine biogeochemistry, on the processes that determine the strength of the carbon pumps that drive the ocean-atmosphere carbon flux, and on the oxygen minimum zones (OMZs) in the ocean. The most pronounced changes occur in the eastern equatorial Pacific (EEP) OMZ, and in the North Atlantic. Changes in global mean values of biological production and export of detritus remain modest, with generally lower values in the mid-Holocene. The simulated ocean-atmosphere CO_2-flux is of the right order of magnitude to explain the observed atmospheric pCO_2 evolution, but with different timing. As the most significant result, we find a substantial increase in volume of the OMZ in the EEP continuing into the late Holocene in the non-accelerated simulation. The concurrent increase of age of the water mass within the EEP OMZ suggests that this growth is driven by a slow down of the circulation in the interior of the deep Pacific. This results in large scale deoxygenation in the deeper Pacific and hence the source regions of the EEP OMZ waters from mid-to-late Holocene. The simulated expansion of the OMZ raises the question whether the currently observed deoxygenation is a continuation of the orbitally driven decline in oxygen, or if it is already a result of the occuring climate change from anthropogenic forcing as widely assumed. An additional explanation would be that the anthropogenic forcing amplifies the natural forcing. The increase in water mass age and EEP OMZ volume can only be simulated with the non-accelerated model simulation. The simulations thus demonstrate that non-accelerated experiments are required for an analysis of the marine biogeochemistry in the Holocene.

1 Introduction

Numerical models that combine the ocean circulation and marine bogeochemistry have been developed since the 1980s (e.g., Maier-Reimer et al., 1993; Maier-Reimer, 1993; Six and Maier-Reimer, 1996; Maier-Reimer et al., 2005). Few studies of marine carbon cycle variability during the Holocene have been performed, however, as the focus of marine carbon cycle research has been more on recent and future climate change related carbon cycle changes (e.g., Maier-Reimer and Hasselmann, 1987; Maier-Reimer et al., 1996), and glacial-interglacial changes (e.g., Heinze et al., 1991). However, one thousand year long transient climate experiments have been performed for the last millennium with Earth system models that include the marine carbon cycle, (e.g., Jungclaus et al., 2010; Brovkin et al., 2010), and more recently the CMIP5/PMIP3 Millennium experiments (Atwood et al., 2016; Lehner et al., 2015)

Of the many features that characterize the biogeochemical system in the ocean, here we will concentrate on oxygen minimum zones (OMZs), ocean-atmosphere carbon fluxes, and the marine ecosystem. OMZs have received particular attention in the recent past. This is in large part due to the observation that in the last five decades, a general deoxygenation of the world's ocean, and an intensification of the ocean's main OMZs has occurred (e.g., Stramma et al., 2008; Karstensen et al., 2008; Schmidtko et al., 2017). A further decrease of oceanic O_2 concentrations has been projected for the future with numerical models (e.g., Matear and Hirst, 2003; Cocco et al., 2013; Bopp et al., 2013) as a consequence of anthropogenic climate change. Knowing the past variations of OMZ extent and oxygen concentrations is, therefore, of immediate relevance to estimate the importance of the observed and projected deoxygenation.

Based on a model study with an intermediate complexity model to investigate glacial-interglacial variations of oxygen, Schmittner et al. (2007) found a causal relation of Indian and Pacific ocean oxygen abundance and a shut down of the Atlantic Meridional Overturning Circulation (AMOC). In their experiments, AMOC variability was generated by freshwater perturbations.

An attempt to better understand the currently observed and future projected expansion of the OMZ based on paleoceangraphic observations (Moffitt et al., 2015) indicates an expansion of

Discussion Paper | Discussion Paper | Discussion Paper | Discussion Paper |

the major OMZs in the world ocean concurrent with the warming since the last deglaciation (18-11 kyr BP). This is based on estimates of seafloor deoxygenation using snapshots at 18, 13, 10, and 4 kyr BP.

Although the focus of this manuscript is on marine biogeochemistry, it is the changes in climate that are driving the changes in marine biogeochemistry in our experiments. Hence, some characteristics of the Holocene climate variability need to be addressed. Model-based investigations of Holocene climate are performed under the auspices of the Paleo Model Intercomparison Project (PMIP, Braconnot et al., 2012). Initially, numerical model time slice experiments have been used to simulate the climate at specific time intervals, typically 9.5 kyr, 6 kyr, and 0 kyr BP (kyr BP = kilo years before present).

Also transient experiments over the entire Holocene have been performed, mainly with accelerated orbital forcing to save computing time (Lorenz and Lohmann, 2004; Varma et al., 2012; Jin et al., 2014) or intermediate complexity models with non-accelerated forcing (Renssen et al., 2005, 2009). In summary the PMIP simulations show a fairly stable global climate with a tendency for warmer mid-Holocene temperatures and colder late Holocene temperatures in particular over land (Wanner et al., 2008).

A second source of information about climate variability during the Holocene comes from proxy data. A concerted effort to synthesize these estimates by the PAGES2K project has resulted in a temperature reconstruction over the last 2,000 years in fairly high temporal resoulution (PAGES 2k Consortium, 2013). In this reconstruction, the global mean surface air temperature is analyzed to cool by about 0.3°C between 1000 A.D. and 1900 A.D, followed by a sharp increase in temperature. Before 1000 A.D. the temperature is fairly constant at about 0.1 °C colder than the 1961-1990 average.

Wanner et al. (2008) also provide a comprehensive overview of globally collected proxy-based climate evolution for the last 6,000 yr together with some instructive plots of the solar insolation changes during that period based on Laskar et al. (2004). For land-based proxies the authors consistently find a decrease of temperatures from 6 kyr BP until now, with different amplitude, but for the ocean this is more heterogenous (Wanner et al., 2008, Fig. 2). E.g., the sea surface temperature (SST) displays an increase with time in the subtropical Atlantic, whereas SST decreases in line with the land surface records in the western Pacific and in the North Atlantic (see also Marchal et al., 2002).

A continuous reconstruction of temperatures for the entire Holocene, i.e., the past 11,300 years, albeit with lower temporal resolution before the PAGES2K period has been assembled by Marcott et al. (2013). In their reconstruction, global mean surface air temperature increases by about 0.6 °C between 11.3 kyr BP and 9 kyr BP to 0.4 °C warmer than present (as defined by the 1961-1990 CE mean). After 6 kyr BP temperatures slowly decrease by 0.4 °C until 2 kyr BP and are relatively stable for 1,000 years. This is followed by a relatively fast decrease beginning around 1 kyr BP of 0.3 °C, in agreement with the PAGES2K data and an increase to present day temperatures in the last few hundred years before present (Marcott et al., 2013, Fig. 1a-f).

The simulated climate and its variability has been compared to proxy data Wanner et al. (e.g., in 2008); Leduc et al. (e.g., in 2010); Emile-Geay et al. (e.g., in 2016). Model simulations and proxy-based estimates of past climate variability apparently show some disagreement, and the model simulations described here make no exception. One reason may be a different behaviour between land and ocean, as e.g., the PMIP2 model simulations shown in Wanner et al. (2008) show warmer mid-Holocene temperatures over land, in particular over Eurasia, whereas there is little SST difference between 6 kyr BP and modern values.

Also on shorter timescales there are descrepencies between model results and proxy-based records. E.g., proxy-based estimates indicate changing El Niño-Southern Oscillation (ENSO) related variability during the Holocene and the proxy-derived inverse relationship between ENSO variability and the amplitude of the seasonal cycle cannot be reproduced by most of the PMIP models (Emile-Geay et al., 2016). The reasons for the mismatch in proxy-based and model-simulated Holocene climate variability, despite some efforts in the PMIP community, have yet to be established.

In this manuscript we aim at closing the gap between glacial-interglacial and future greenhouse gas driven simulations of climate and the marine carbon cycle. Following earlier time slice experiments with a coupled atmosphere-ocean-sea ice climate model and a marine biogeochemistry model (Xu et al., 2015), here we are using transient model simulations with such a model system that are covering the last 9.5 kyr of the Holocene. In particular, we investigate the temporal evolution of some of the key elements of the simulated climate that are important drivers of marine biogeochemistry variations, such as SST and AMOC. For the marine carbon cycle we focus on global values of primary production, export production, and calcite export, all of which can be important drivers of the atmosphere-ocean CO_2-flux and OMZ variations. Based on these results we analyse and discuss i) changes in the OMZs, in particular in the EEP but also in the Atlantic and the Arabian Sea, ii) whether the integrated effect of changes in the ocean-atmosphere CO_2-flux can explain the reconstructed atmospheric pCO_2 during the Holocene, and iii) changes in the marine ecosystem.

In addition we want to address the more technical question to what extent simulations with accelerated orbital forcing are suitable for Holocene marine biogeochemistry simulations. In the accelerated-forcing experiments, the change in orbital parameters between two model years corresponds to a 10 yr step in the real orbital forcing (see Sec. 2.2.1). For climate simulations, the sensitivity to accelerated vs. non-accelerated forcing has recently been investigated for the last two interglacials (130-120 kyr BP and 9-2 kyr BP, Varma et al., 2016), indicating that non-accelerated experiments differ from accelerated experiments in the representation of Holocene climate variability in the higher latitudes of both hemispheres while the behaviour is more similar in low latitudes. A different temporal evolution was also found for the deep ocean temperature, with the non-accelerated experiment displaying a larger variation. Here we perform and analyse simulations of the marine biogeochemisry of the Holocene forced by an accelerated and a non-accelerated climate model simulation of the Holocene.

We will first describe the numerical models, the experiment setup, and characteristics of the time-varying forcing in Sec. 2, report the results for climatic and biogeochemical variables in Sec. 3, and discuss the results and implications for future research in Sec. 4.

Biogeosciences Discuss., https://doi.org/10.5194/bg-2017-554
Manuscript under review for journal Biogeosciences
Discussion started: 4 January 2018

2 Model description and experiment set-up

2.1 Models

2.1.1 The Kiel Climate Model (KCM)

Oceanic physical conditions are obtained from the global coupled atmosphere-ocean-sea ice model KCM (the Kiel Climate Model, Park and Latif, 2008; Park et al., 2009), in particular from NEMO/OPA9 (Madec, 2008), which comprises the oceanic component of KCM and includes the LIM2 sea ice model (Fichefet and Morales Maqueda, 1997). The atmospheric component is ECHAM5 (Roeckner et al., 2003). The spatial configuration for ECHAM5 is T31L19, and for NEMO the ORCA2 configuration is chosen, i.e., a tripolar grid with a nominal resolution of 2°x 2°and a meridional refinement to 0.5°near the equator and 31 layers with a finer resolution in the upper water column.

KCM has previously been used to conduct and analyse time-slice simulations of the pre-industrial and the mid-Holocene climate and hydrological cycle (Schneider et al., 2010; Khon et al., 2010, 2012; Salau et al., 2012) and contributed to PMIP3 (e.g., Emile-Geay et al., 2016). More recently, orbital forcing (eccentricity, obliquity, and precession) were varied continiously over the last 9,500 yr of the Holocene according to the standard protocol of PMIP (Braconnot et al., 2008). This forcing was accelerated by a factor of 10, resulting in a transient model experiment of 950 model years for the Holocene (Jin et al., 2014). Here, in additional KCM experiments, the forcing is non-accelerated, so that the Holocene is represented by 9,500 model years starting from 9.5 kyr BP (see Sec. 2.2.1 for the experiment description).

2.1.2 Pelagic Interactions Scheme for Carbon and Ecosystem Studies (PISCES)

Monthly mean fields of temperature, salinity, and the velocity from the KCM experiment were used in off-line mode to force a global model of the marine biogeochemistry (PISCES, Aumont et al., 2003).

Since the description of PISCES in Aumont et al. (2003) is quite comprehensive, we restrict the model description to the most relevant parts for our investigation. Sources of oceanic oxygen are gas exchange with the atmosphere at the surface, and biological production in the euphotic zone. Oxygen consuming heterotrophic aerobic remineralization of dissolved organic carbon (DOC) and particulate organic carbon (POC) is simulated over the whole water column, i.e., also in the euphotic layer. Remineralization depends on local temperature and O_2-concentration. For an increase of 10 °C the rate increases by a factor of 1.8 (Q_{10}=1.8). Remineralization is reduced for O_2-concentrations below 6 μmol l^{-1}.

Primary production is simulated by two phytoplankton groups representing nanophytoplankton and diatoms. Growth rates are based on temperature, the availability of light and the nutrients P, N (both as nitrate and ammonium), Si (for diatoms), and the micronutrient Fe. The elemental ratios of iron, chlorophyll, and silicate within diatoms are computed prognostically based on the surrounding water's concentration of nutrients. Otherwise they are constant following the Redfield ratios. Photosynthetically available radiation (PAR) is computed from the shortwave radiation passed from ECHAM to NEMO. Sea ice is assumed to reflect all incoming radiation so there is no biological production in areas that are completely sea ice covered (i.e., where the sea ice fraction is equal to 1).

There are three non-living components of organic carbon in PISCES: semi-labile DOC, as well as large and small POC, which are fuelled by mortality, aggregation, fecal pellet production and grazing. In the standard version of PISCES, large and small POC sinks to the sea floor with their respective settling velocities of 2 and 50 md^{-1}. For large POC, the settling velocity increases further with depth. In the model version employed here, simulation of the settling velocity of large detritus is formulated allowing for the ballast effect of calcite and opal shells according to Gehlen et al. (2006) while the settling velocity of small POC remains constant at 2 md^{-1}. In most areas and at most depths, this leads to a reduction of the settling velocity for large POC compared to the (50 md^{-1} and more) standard version. The new formulation of the settling velocity for large POC generally improved the oxygen fields of the KCM-driven PISCES simulation compared to modern day WOA data (Garcia et al., 2013), in particular in the EEP (see Appendix A for a comparison of observed and simulated oxygen distribution and a sensitivity of the OMZ volume to the O_2-threshold). Note that the ballast parameterization

Biogeosciences Discuss., https://doi.org/10.5194/bg-2017-554
Manuscript under review for journal Biogeosciences
Discussion started: 4 January 2018

was not part of the PISCES version used in Xu et al. (2015), and therefore the mean state of the EEP OMZ differs between the experiments of Xu et al. (2015) and the ones described here.

We also added an age tracer to PISCES. The age tracer is set to zero at surface grid points, and then the age increases with model time elsewhere. Advection and mixing is also applied to the age tracer.

2.2 Experiment setup

2.2.1 KCM - greenhouse gases and astronomical forcing (KCM-CTL, KCM-HOLx10, and KCM-HOL)

As greenhouse gas and orbital forcing are the main boundary conditions driving the forced variations in the KCM experiments, we describe this forcing in a little more detail.

Prescribed atmospheric CO_2 concentration (Fig.1a) varied from 263.7 ppm at the beginning of the Holocene, decreased to 260 ppm around 7 kyr BP in the mid-Holocene, and then increased to about 274 ppm for the present day pre-industrial conditions (based on Indermühle et al., 1999). CH_4 and N_2O were kept at constant levels of 678.8 ppb and 260.6 ppb, respectively, in all KCM experiments.

Eccentricity remained fairly constant at a value of 0.02 over the entire Holocene. The precessional index increased from -0.015 to 0.02, and the obliquity decreased from about 24.2°to 23.5°. In general, this leads to less insolation during northern hemisphere summer, and more insolation in southern hemisphere summer: Solar radiation at the top of the atmosphere (TOA) in June decreased during the Holocene from 9.5 kyr BP to 0 kyr BP by about 25 Wm^{-2} at the equator and 45 Wm^{-2} at 60°N. On the southern hemisphere, the decrease is up to 10 Wm^{-2} at 30°S, and at 60°S there is a weak increase of a few Wm^{-2}. In December the insolation is stronger for 0 kyr BP than for 9.5 kyr BP by up to 30 Wm^{-2} at 30°S and about 5 Wm^{-2} at 60°N (see also Jin et al. (2014, Fig. 2) and Wanner et al. (2008, Fig. 6) for changes in solar radiation at top of atmosphere vs. time for different latitudes and summer/winter, based on Berger and Loutre (1991) and Laskar et al. (2004), respectively).

We note that the total annual radiation driven by precession changes remains fairly constant at each latitude and globally, whereas obliquity changes cause changes also in the annual mean insolation (see e.g., Fig.1b in Schneider et al., 2010). These annual mean changes in TOA insolation from 9.5 kyr BP to 0 kyr BP are an increase of around 5 Wm^{-2} at the poles and a decrease of 1 Wm^{-2} at the equator, thereby potentially decreasing the latitudinal temperature gradient.

For our analyses that focus on ocean physical conditions and marine biogeochemistry, however, we need to consider the TOA forcing as filtered by the atmosphere (i.e., the atmospheric component of KCM). In Fig. 1b annual and zonal mean anomalies of short wave radiation (SWR) at the ocean and sea ice surface are displayed as a Hovmöller diagramme. These annual mean anomalies are somewhat different from the TOA anomalies, but more relevant to understand the simulated SST evolution and changes in PAR. In the early Holocene, negative anomalies of -1 to -3 Wm^{-2} develop at high latitudes of mainly the southern hemisphere. In the mid-Holocene negative anomalies of -1 to -3 Wm^{-2} start to evolve also in northern high latitudes, and are -3 to -5 Wm^{-2} in the southern high latitudes around 60°S, whereas SWR-anomalies become positive in low latitudes (1 to 3 Wm^{-2}). At around 60°N, there is a shift from negative to positive anomalies at around 6.8 kyr BP. During the late Holocene, the positive anomalies in the low latitudes intensify (3 to 5 Wm^{-2}), whereas the high latitude anomalies remain about constant.

All KCM experiments discussed here were started from year 2,000 of a spin-up experiment forced by 9.5 kyr BP astronomical forcing and atmospheric pCO_2 (263.8 ppm). The spin-up experiment itself was started from a KCM experiment with constant 9.5 kyr BP orbital forcing but present day pCO_2 (286.4 ppm). The KCM control experiment (KCM-CTL) was integrated for a further 2,000 years with orbital parameters and atmospheric pCO_2 (263.8 ppm) kept constant at 9.5 kyr BP values as continuation of the spin-up experiment. In experiments KCM-HOLx10 and KCM-HOL, time varying orbital forcing (Berger, 1978) and green house gases (Braconnot et al., 2012) were applied as forcing.

2.3 Spin-up of PISCES and control experiment (BGC-CTL)

To spin up the biogeochemical model, monthly mean ocean model output from experiment KCM-CTL was used as forcing. This 2,000 yr long forcing was repeated three times to spin-up PISCES for 6,000 years, after which period the model drift as defined by air sea carbon flux and age of water masses was negligible. It was in particular the age tracer in the deep northern Pacific that required the long spin-up time. Note that this spin-up simulation does not achieve a 'classical' time-invariant steady state but reflects the internal variability of the 2,000 year experiment KCM-CTL and any remaining drift. After repeating the KCM-CTL forcing three times for the spin-up, PISCES was integrated for a further 2,000 years with the KCM-CTL forcing as a control experiment for the marine biogeochemistry (BGC-CTL).

2.4 Transient experiments with PISCES (BGC-HOLx10, BGC-HOL)

Similarly to the set-up of the Holocene KCM experiments, we performed two transient experiments with PISCES in off-line mode. Both transient experiments are also started from year 6,000 of experiment BGC-CTL. In the accelerated experiment BGC-HOLx10, oceanic fields of KCM-HOLx10, and the same atmospheric pCO_2 as in KCM-HOLx10 is prescribed as forcing. In this experiment, PISCES is integrated for 950 years corresponding to the period 9.5 kyr BP to 0 kyr, with 10-fold accelerated forcing. Monthly mean output is stored.

The non-accelerated experiment BGC-HOL is also started from year 6,000 of BGC-CTL, but is integrated for 9,500 years forced by the non-accelerated experiment KCM-HOL and the corresponding pCO_2. All experiments and their names are sumarized in Tab. 1.

Note that the approach here differs from earlier work to investigate Holocene OMZ changes with a KCM/PISCES model setup, where PISCES was forced by PMIP-protocol time-averaged oceanic conditions for specific time slices (6 kyr BP and 0 kyr BP, Xu et al., 2015). Also, now all BGC experiments make use of the direct KCM-NEMO output, as opposed to the setup in Xu et al. (2015) where KCM-derived anomalies were added to mean ocean fields from an reanalysis-forced ocean-only setup.

3 Results

All plots in the results section are based on model output interpolated to a regular 1°x 1°grid, with the exception of the meridional overturning circulation that has been computed on the original ORCA2 grid. For all time series the time-axis represents the forcing years. This corresponds to model years for the non-accelerated experiments but not for the accelerated experiments, so any variation caused by long term internal variability of the model would be spread out in time in the accelerated experiment compared to the non-accelerated experiment. For all time series, the long term changes are indicated by the 4th order polynomial fits. Polynomial fits were chosen over running averages to also include the end points of the simulation. Dots represent annual averages and their spread indicates shorter time scale variability. Plots for BGC-HOL are based on output from every 10th year, both to be consistant with BGC-HOLx10, and to keep the output file size at a managable level. For BGC-CTL, only annual averages are shown (also every 10th year). Due to some interesting but spurious behaviour of the marine biogeochemistry, we excluded the Mediterranean Sea from the analysis by masking it out.

3.1 Climate variations over the Holocene

Since the biogeochemical variations depend to a large extent on the changes in ocean physics, we will first examine the relevant aspects of the simulated climate variations over the Holocene.

3.1.1 Sea surface temperature

As a first indicator of simulated changes in ocean physics, we present time series of the global and annual mean SST (Fig. 2a). The global mean SST in KCM-HOL is 15.1 °C at 9.5 kyr BP, decreases to 14.8 °C at 6.5 kyr BP, and increases again to 15.6 °C at 0 kyr BP. In KCM-HOLx10, the temporal evolution is similar as in KCM-HOL, but with a smaller decrease of global mean SST in the early Holocene (to 15.0 °C and a slightly higher SST than KCM-HOL at the end of the late Holocene (15.7 °C).

We note that also the control experiment KCM-CTL displays a modest decrease of global mean SST (about 0.1 °C per 1,000 years over its 2,000 yr integration time), implying that the simulated early Holocene decrease in SST in KCM-HOL and KCM-HOLx10 is the combined result of a remaining model drift, and the orbital and CO_2 forcing.

A Hovmöller diagramme of zonal mean SST anomalies of KCM-HOL (Fig. 2b) reveals that the mid-Holocene cooling is strongest in the higher latitudes of the southern hemisphere (up to -0.75 °C, centered at around 60°S) whereas the late Holocene warming is strongest between 40°S and 40°N. with maxima around the equator and at 40°S. This pattern coincides to large extent with that of the anomalies of SWR at the ocean and sea ice surface (Fig.1b).

The seasonal cycle of global mean SST in KCM-HOL doubles its amplitude from around 0.35 °C in the early Holocene to 0.7 °C at about 3 kyr BP (Fig. A.3a), indicating the dominance of the increasing seasonal cycle in the solar forcing on the southern hemisphere mid latitudes over the decreasing seasonal cycle on the northern hemisphere (Jin et al., 2014). The seasonal cycle of global mean SST remains in the range of slightly less than 0.7 °C during the late Holocene after 3 kyr BP.

3.1.2 Atlantic meridional overturning circulation

The AMOC serves as an indicator of the intensity of deep water formation in the source region of the global conveyor belt. AMOC has been computed here with the standard cdf-tool that is available from the NEMO-package (available from https://github.com/meom-group/CDFTOOLS). From this output, maximum AMOC at 30°N has been computed and, for better readability, 100 yr running means are shown in Fig 3. The simulated maximum AMOC at 30°N in KCM-HOL at the beginning of the Holocene is around 14.5 Sv. During the Holocene the 100 yr running mean AMOC is gradually decreasing to slightly more than 12.5 Sv during the first half of the Holocene, indicating a weak slow down of the global conveyor belt circulation. AMOC then slightly intensifies again but only marginally until the end of the Holocene to around 12.5 Sv (Fig.3). In KCM-HOLx10 the mean AMOC and its temporal evolution are similar to KCM-HOL, with a slightly higher mean value. Overall, the long term changes in AMOC are relatively small and remain within the range of interannual variations of around 2-3 Sv.

3.1.3 Age of water masses

In addition to AMOC, the age of water masses can serve as an indicator of deep water formation, the intensity of the global deep water circulation, and help to understand changes in oxygen concentration. We will investigate time series of the water mass age in the deep ocean at the source and end regions of the global convyeor belt circulation, namely the North Atlantic and the North Pacific. The renewal of water masses in the North Atlantic is indicated by a time series of the age tracer averaged between 1,800 m and 2,500 m depth and 40°W to 10°W, 40°N to 60°N in Fig. 4a. The average water mass age in this volume in BGC-HOL initially ranges from 60 to 80 yr over the first 2,800 yr, followed by a sudden decrease to slightly more than 25 yr that occurs within a few yr around 6.8 kyr BP. This is followed by a gradual increase to around 40 yr over the remaining 6,800 yr of the Holocene. The sudden decrease is likely driven by changes in SST in the North Atlantic which in turn are a consequence of the changing solar radiation in this area. We will come back to this point in Sec. 3.2.6. In the accelerated experiment BGC-HOLx10 (brown curve in Fig. 4a) a slightly weaker decrease in age from 60 to 30 yr is simulated for the deep North Atlantic, but it occurs over a longer time period (roughly 300 model years) and later in terms of forcing years (between 4 kyr and 1 kyr BP).

At the far end of the conveyor belt circulation, the deep North Pacific, changes occur less sudden than in the North Atlantic, but with a larger amplitude. Between 2,500 m and 3,500 m depth, 150°E to 130°W, 40°N to 60°N the water masses show an initial age of 1,475 yr for all experiments (Fig. 5). In BGC-HOL, water mass age initially decreases to around 1,400 yr around 7.5 kyr BP, but from thereon there is a steady increase up to an age of 1,800 yr at the end of the Holocene. This can not be simulated in the accelerated experiment BGC-HOLx10, however, that runs for 950 yr only. In BGC-HOLx10 deep North Pacific water mass age decreases slightly stronger than in the control experiment to 1,400 yr at 0 k BP. The increase in water mass age in the non-accelerated experiment BGC-HOL is indicating a considerable slow down of the global conveyor belt circulation over the Holocene with significant impact on the marine biogeochemistry in the Pacific. We will come back to the age of water masses when investigating the evolution of the EEP OMZ in section 3.2.5.

3.2 Biogeochemical variations

3.2.1 Ocean-Atmosphere carbon flux

The global mean ocean-atmosphere carbon flux provides a measure on whether the ocean acts as a carbon source or sink to the atmosphere. In the early Holocene this flux is around -0.5 GtC yr^{-1} (Fig. 6a), the equilibrium value in the PISCES model, balancing riverine carbon input. In the mid-Holocene the outgassing is slightly reduced to around 0.4 GtC yr^{-1}. Indicating slightly stronger outgassing, the value increases to -0.75 GtC yr^{-1} in the late Holocene in experiment BGC-HOL, whereas it remains at around -0.4 GtC $yr^{-}1$ in experiment BGC-HOLx10. At the same time, the amplitude of the seasonal cycle of the atmosphere-ocean carbon flux in BGC-HOL decreases from early to late Holocene from around 1.8 GtC yr^{-1} to only 0.8 GtC yr^{-1} (Fig. A.3b).

Fig. 6a indicates that a weak oceanic source of CO_2 could have been contributing to the increasing atmospheric pCO_2 towards the end of the Holocene. Fig. 7 shows the diagnosed temporal evolution of atmospheric pCO_2 as calculated from the time integrated ocean-atmosphere CO_2 flux in experiment BGC-HOL (dashed curve), together with the reconstructed pCO_2 from Indermühle et al. (1999) as in Fig. 1a. The decrease of pCO_2 occurs later in time, and the increase towards the late Holocene is faster than reconstructed, but the range is of the same order of magnitude. We will come back to this point in the discussion.

3.2.2 Surface alkalinity and pH

The global mean concentration of total alkalinity (TA) in the control run is 2250-2258 μmol l^{-1} (Fig. 8a). In BGC-HOL it increases to 2260 μmol l^{-1} (around 7 kyr BP) and 2280 μmol l^{-1} in the late Holocene (0 k), a value that is closer to the present day observed value of 2300 μmol l^{-1} (GLODAP, Takahashi et al., 2014). In experiment BGC-HOLx10 the global mean concentration of TA remains in the range of the control run, with a maximum at around 6 kyr BP. The increase in TA in BGC-HOL occurs over most latitudes (Fig. 8b) with a stronger increase north of 40°N and around the equator between 5 kyr BP and 3 kyr BP. There is only a small trend around

60°S. This temporal evolution can only partly be explained by a reduction in $CaCO_3$ export that would drive an increase in TA (Sec. 3.2.4, Fig. 12b).

The global and anual mean pH at the surface is following the temporal variations in atmospheric pCO_2 and varies only little during the Holocene, with changes in the range of a few hundredths pH-units (8.13 - 8.16, not shown).

3.2.3 Nutrients

In BGC-HOL, the global mean NO_3 concentration averaged over the euphotic zone (0-100 m) is decreasing with time from 56 μmol l^{-1} in the early Holocene to 52 μmol l^{-1} around 3 kyr BP. This is followed by a slight increase to almost 53 μmol l^{-1} at 0 kyr BP (Fig. 9a). In BGC-HOLx10, the global mean concentration is fairly constant at 56 μmol l^{-1} until 5 kyr BP, and then declines gradually to 54 μmol l^{-1} in the late Holocene. The Hovmöller diagramme of the zonal mean NO_3 concentration anomalies (average of the first 200 years subtracted) of experiment BGC-HOL (Fig. 9b) reveals that the decrease of the NO_3 concentration originates from a large range of latitudes mainly in the southern hemisphere (40°S to 60°S), and also from high northern latitudes after the 'event' around 6.8 kyr BP in the North Atlantic, centered at 60°N. The weak increase of global mean euphotic-zone NO_3 concentration after 3 kyr BP originates mainly from a small band centered at 55°N and a weakening of the negative anomalies around and south of the equator (10°N to 20°S).

3.2.4 Marine ecosystem

Three components of the marine ecosystem are of major relevance relevance for the carbon cycle, namely the integrated primary production, the export production, and the calcite export. The primary production integrated over the euphotic zone (INTPP) is a measure of the productivity of the marine ecosystem. INTPP in BGC-HOL is around 44 GtC yr^{-1} at the beginning of the Holocene, decreasing to a minimum of around 41 GtC yr^{-1} in the mid-Holocene at 5 kyr BP, and then increasing again to 44 GtC yr^{-1} towards the late Holocene (Fig.10a). Interannual variations are about 2-3 GtC yr^{-1}. In the accelerated experiment BGC-HOLx10, INTPP remains fairly constant over the entire Holocene at 43 to 44 GtC yr^{-1}, which is similar to the range of the control experiment BGC-CTL.

The decrease in global mean INTPP in BGC-HOL originates mainly from latitudes south of 40°N and is more pronounced on the southern hemisphere (Fig.10b). The increase after 4 kyr BP can be traced back to an increase in INTPP between 40°N and 60°N beginning around 6 kyr BP and intensifying and spreading southward gradually for the remainder of the Holocene. This response is likely a combination of the changes in PAR, SST, and nutrient availability (Figs. 1b, 2b, 9b), as there is some similarity between zonal mean anomalies of INTPP and SST, SWR at the sea/ice surface, and NO_3, but none of the patterns is matched excactly.

The export production at 100 m depth in BGC-HOL, here as sum of small and large POC, is around 10.2 GtC yr^{-1} at 9.5 kyr BP. During the late and mid-Holocene, there is a slight decrease to 9.8 GtC yr^{-1} at 4 kyr BP. Export production remains fairly constant at that level until 1 kyr BP after which there is a modest increase to 10 GtC yr^{-1} (Fig.11a). The accelerated experiment BGC-HOLx10, after an small increase in the early Holocene, simulates a relatively uniform decrease in export production from 8 kyr BP to 0 kyr BP.

The zonal mean export production in BGC-HOL decreases mainly in the low latitudes in two bands centred around 20°N and 35 °S (Fig.11b). An increase occurs mainly between 30°N and 60°N, intensifying after 6.8 kyr BP. The apparent deviations from the pattern of INTPP100 could be explained by changing temperatures (with an impact on the remineralizaion rate) and changes in the particle composition (with an impact on settling velocity) and relative contributions from small and large POC to the export production. For slowly sinking small POC, we find a more continuous but minor decline of global export from 3.7 to 3.6 GtC yr^{-1}, whereas for the faster sinking large POC the decline is more rapid during the first 3,000 yr of the Holocene (from 6.5 to 6.3 GtC yr^{-1}) and the export is fairly constant thereafter (not shown).

The temporal evolution of the calcite export in all experiments is similar to that of INTPP: In BGC-HOL, calcite export is around 1.08 GtC yr^{-1} in the early Holocene (Fig.12a), followed by a decrease of about 0.1 GtC yr^{-1} (10%) until the mid-Holocene (around 6 kyr BP) after which there is a slight increase again to 1.05 GtC yr^{-1} towards the late Holocene. In BGC-HOLx10 and BGC-CTL, the calcite export fluctuates around its initial value of about 1.08 GtC yr^{-1}

fairly constantly. The zonal mean changes of $CaCO_3$ export in BGC-HOL are similar to that of INTPP, with an almost global decrease in the early Holocene, and a recovery in the higher northern latitudes after 6.8 kyr BP, that gradually extends to the enire northern hemisphere in the late Holocene (Fig.12b).

Overall the variations of the global production and export rates remain small throughout the Holocene even in the non-accelerated experiment BGC-HOL, with a tendency for lower values in the mid-Holocene.

3.2.5 Oxygen minimum zones

The main OMZ in the global ocean resides in the EEP, the latter is here defined as the region from 140°W - 74°W, 10°S-10°N. Hence, we will first investigate this region. Fig. 13 displays the temporal evolution of the EEP OMZ as simulated for the Holocene. The volume of the EEP OMZ, as defined by a 30 μmol l^{-1} threshold, initially remains fairly constant in KCM-HOL from 9.5 kyr BP to 7 kyr BP at $15\times10^{14}m^3$. But from 7 kyr BP onwards, the OMZ volume steadily increases to around 26 $\times10^{14}m^3$ at 0 kyr BP in KCM-HOL, an increase of more than 70%. In the accelerated forcing experiment KCM-BGCx10 the EEP-OMZ volume remains fairly constant over the entire Holocene. At the same time as the OMZ volume increases in KCM-HOL, the age of the water mass within the OMZ increases from around 440 yr (9.5 - 7 kyr BP) to 530 yr at 0 kyr BP in experiment KCM-HOL, whereas it decreases slightly in BGC-HOLx10. Also the control run does not show substantial variations of OMZ volume and water mass age. The average O_2 concentration within the OMZ decreases slightly from 18.5 μmol l^{-1} at 9.5 kyr BP to 17.5 μmol l^{-1} at 0 kyr BP in KCM-HOL (not shown).

Note that the accelerated experiment does not show an increase in the OMZ volume and water mass age (Fig. 13). As the age of the water increases in the non-accelerated experiment, more organic material that is raining down from the surface will be remineralized in a given water volume, thereby reducing its oxygen concentration. Export production in the EEP is fairly constant over the Holocene at 0.58 GtC a^{-1}(figure not shown), with only a marginal tendency for lower values in the late Holocene, and thus can be ruled out as a driver of the expansion of the EEP OMZ.

In contrast, for the OMZ in the tropical Atlantic mainly south of the equator, the changes over the Holocene are more modest and of opposite sign. In the region from 5°W - 15°E, 30°S - 5°N, the volume of the OMZ in BGC-HOL decreases slowly from around 4 x 10^{12}m^3 to 3.5 x 10^{12}m^3, and the average age over the OMZ decreases from about 125 yr to 115 yr (Fig. 14).

For the Arabian Sea there is a small increase in OMZ volume from mid-to-late Holocene in BGC-HOL (4.4 x $10^{12}m^3$ to 4.7 x $10^{12}m^3$), concurrent with an increase in water mass age from 320 to 360 yr (Fig. 15). In the accelerated experiment BGC-HOLx10, on the contrary, there is a decrease of both OMZ-volume and mean water mass age mainly after 4 kyr BP. Also BGC-CTL displays a decrease in average water mass age for the Arabian Sea, whereas the OMZ-volume remains about constant. Note that the results for the Arabian Sea in Gaye et al. (2017, BGD, accepted for BG) are from an earlier version of BGC-HOLx10, started at year 1,500 of KCM-CTL, and, therefore, are not directly comparable.

3.2.6 North Atlantic

Our original intention in examining the North Atlantic more closely was to investigate whether the changes in the OMZs could be traced back to the deep water source regions. It turned out, however, that significant changes occurred in the North Atlantic, that justify further analysis. In section 3.1.3 we showed a sudden drop in the water mass age in the deep North Atlantic (Fig. 4a) that can be traced back to a westward shift in the deep water formation areas south of Iceland, and a northward shift north of Iceland, as indicated by the difference in the annual maximum of the mixed layer depth in the North Atlantic (Fig. 4b). In addition to the shift of location, also an increase of the mixed layer depth of up to 3000 m occurs in the more southwestern part of the Nordic Seas. This is accompanied by a change in SST at 60°N around 6.8 kyr BP from negative to positive anomalies (Fig. 2b), and an increase in export production (Fig.11b).

Fig. 1b reveals a shift from negative anomalies of annual mean SWR at the ocean/seaice surface just north of 60°N to positive anomalies in a narrow band south of 60°N, and a negative anomaly north of 75°N. In particular the positive anomaly south of 60°N seems surprising, as TOA radiation in the North Atlantic is decreasing from 9.5 kyr BP to 7 kyr BP from around 190 W m^{-2} to 180 W m^{-2}. This decrease is more pronounced in summer, with a potential

Biogeosciences Discuss., https://doi.org/10.5194/bg-2017-554
Manuscript under review for journal Biogeosciences
Discussion started: 4 January 2018

for preconditioning the water masses for winter convection, whereas winter insolation is very low anyway so any changes would be of limited impact. The TOA SWR northern hemisphere decrease is fairly linear and continues further for the entire Holocene. The abrupt response of KCM to the forcing anomalies suggests that there may be a critical threshold for a sudden shift of deep water formation areas in the (model) North Atlantic during the Holocene.

This shift is also visible in the concentration of NO_3 (Fig. 9b) and the marine ecosytem as indicated by INTPP, and export production that both increase south of 60°N after 6.8 kyr BP and decrease north of 65°N (Figs. 10b, 11b).

4 Discussion

Comparing the temporal evolution of global mean SST with observation-based estimates and other model simulations, there is a notable difference with observations. During the well established climate optimum in the mid-Holocene (8 kyr to 5 kyr BP) observation based global mean temperature is about 0.4 °C warmer than 1961-1990 (Marcott et al., 2013), and borehole temperatures from Greenland are about 2 °C warmer (Dahl-Jensen et al., 1998). During the same period the KCM-simulated SST is at its lowest value, about 0.8 °C colder than at the end of the simulation at 0 kyr BP in the non-accelerated experiment (Fig. 2).

The largest fraction of the initial post-glacial temperature increase in the reconstructions of Marcott et al. (2013), however, occurs in the very early Holocene (11.3 kyr BP to 9 kyr BP), whereas the simulations discussed here start at 9.5 kyr BP to avoid difficulties with the simulation of retreating ice masses and increasing sea level. Simulations, therefore, start at a time when continental ice sheets and sea level are assumed to be close to present day values. This very early Holocene temperature increase can, therefore, not be simulated by KCM in its present configuration. We note that also in the Holocene time slice experiments with KCM, the annual mean SST is lowest for the 6 kyr BP experiment, and highest for the 0 kyr BP experiment (e.g., Schneider et al., 2010, Fig.6).

In support to our model results, Varma et al. (2016) find a similar temporal evolution of global mean SST in their orbitally forced Community Climate System Model version3 simulations of the Last and Present Interglacials (LIG and PIG, respectively) mainly in their non-accelerated PIG experiment (their Fig.4). The larger amplitude of our simulated temperature change can be explained by the small cooling trend still inherent in the control run (KCM-CTL, about 0.1 °C/ 1,000 years, an otherwise very acceptable value) and the additional forcing from the transient CO_2 variations in KCM-HOL and KCM-HOLx10 (with a range of about 20ppm, Fig. 1a), whereas Varma et al. (2016) used constant pCO_2 values during their simulations.

We also performed an additional transient non-accelerated KCM experiment with constant pCO_2 of 286.4 ppm but orbital forcing for the Holocene that has not been discussed here. In that experiment, the global mean SST fluctuates within a constant range almost until 4 kyr BP, i.e., with no mid-Holocene cooling, and increases by 0.2 °C to 0.3 °C from 4 kyr BP to 0 kyr BP. This indicates that the early to mid-Holocene SST evolution in KCM-HOL is a result of the pCO_2 forcing, whereas for the late Holocene pCO_2 and orbital forcing drive an increase in SST.

We note that also in the simulations of Varma et al. (2016) seemingly small variations in atmospheric pCO_2 lead to larger variations in the simulated global mean SST than expected climate sensitivity estimates derived from idealized pCO_2 increase experiments. For their PIG and LIG simulations with atmospheric pCO_2 of 280 ppm and 272 ppm, respectively, the initial global mean SST difference is more than 0.35 °C. This sensitivity is of similar magnitude as the 0.6 °C for KCM control simulations with a pCO_2 of 286.4 ppm and 263 ppm. Climate sensitivity on very long time-scales for relatively modest atmospheric pCO_2 concentrations seems to warrant further investigation.

The discrepancy between simulated SST, and proxy-based estimates, moreover, raises the question of why the simulations result in such a different temporal evolution than observation based temperature reconstructions. Possibly there might be a difference in the behaviour of the SST and the mainly land-based temperature reconstructions. E.g., Renssen et al. (2009) display simulated differences between 9 kyr BP and 0 kyr BP, and their Fig. 3c suggests mainly colder temperatures of the northern hemisphere oceans for 9 kyr BP, whereas the trend is opposite for the land surface mainly in Eurasia. This could also imply that at least early Holocene temperature variations where determined not only by orbital forcing or CO_2 but also by solar and volcanic forcing, ice sheets, and internal variability of the system (see also Wanner et al. (2008); Renssen et al. (2009) for a more complete and regional investigation of driving mechanisms of Holocene climate).

Turning to the large scale oceanic circulation, the slow down of the circulation in the deep Pacific in experiment KCM-HOL as indicated by the increase in water mass age (Fig. 5) seems stronger than one would expect from the at most 1 Sv/10% decrease of the AMOC (see section 3.1.2). This suggests a decoupling of the North Atlantic and the North Pacific over the course of the Holocene simulations, indicating that changes in the ’far-end’ conveyor belt circulation are not necessarily represented by changes in AMOC. Also Renssen et al. (2005) find in their experiments with a coupled intermediate complexity model that AMOC remains constant throughout their 9,000 yr Holocene experiment, despite changes in the location of the deep water formation regions.

So how would such a slow down in circulation impact on the oceanic oxygen distribution, and how does it relate to current deoxygenation research? A deoxygenation of the global ocean has been observed over the last 50 years (-2% globally, Schmidtko et al., 2017). A further decline of the oxygen content, and hence an extension of the world’s OMZs has been projected in ocean and Earth system model simulations of the next century as a consequence of global warming (Matear and Hirst, 2003; Cocco et al., 2013; Bopp et al., 2013).

As the non-accelerated experiment over the Holocene yields an expanding OMZ in the EEP, and in general declining oxygen concentrations as a result of the natural forcing only, this raises the question whether the presently observed deoxygenation might also partly be caused by the continuation of an naturally forced trend. This would not have to be in contradiction with an anthropogenic contribution to the observed oxygen decline, but could also point to an amplification of the naturally forced trend by the effects of anthropogenic warming as both mechanisms point in the same direction.

Thus, the dominant mechanisms for past and future OMZ-variability have yet to be established. Potential candidates are i) changes in export production, setting the amount of detritus that can be remineralized, ii) temperature changes that effect oxygen solubility and organic matter remineralization, and iii) circulation changes, setting the rates by which deoxygenized water

Biogeosciences Discuss., https://doi.org/10.5194/bg-2017-554
Manuscript under review for journal Biogeosciences
Discussion started: 4 January 2018

masses can be replenished.

The importance of these mechanisms may well change with the time scale considered. Deutsch et al. (E.g., 2011) analyse an ocean general circulation model forced by atmospheric reanalysis from 1959-2005 to identify the main mechanism for oxygen mimimum zone variability in the more recent past. From the analyses the authors find that downward shifts of the thermocline and hence an uplifting of the Martin curve (Martin et al., 1987), resulting in higher respiration rates at the same water depth, drive an increase of the suboxic volume, whereas upwards shifts of the thermocline cause decreasing suboxic volume.

On glacial to interglacial time scales, on/off changes of the AMOC have been identified to drive OMZ variations also in the Pacific (Schmittner et al., 2007). In their model experiments with the UVic (University of Victoria) intermediate complexity model, however, the AMOC collapses entirely, whereas the AMOC in our Holocene simulations varies only by around 10%. As such we find no indication for a direct connection between AMOC changes and the EEP OMZ for more modest changes in AMOC. The mechanism in our transient non-accelerated Holocene experiment is a slowdown of the circulation more confined to the deep Pacific and hence widespread oxygen consumption with an effect on the EEP OMZ (Fig. 13) where the deep waters are upwelled. In the Atlantic, circulation changes remain small over the Holocene, and the oxygen concentration remains fairly constant in the Atlantic OMZ (Fig. 14).

Concerning the observed changes in atmospheric pCO_2 over the Holocene, Indermühle et al. (1999) postulate that changes in the terrestrial biosphere and SST were driving the observed changes. Elsig et al. (2009) base their investigation on $\delta^{13}C$ measurements from an Antarctic ice core. They attribute the 5 ppm early Holocene decrease in atmospheric pCO_2 to an uptake of the land biosphere, and the mid-to-late Holocene increase of 20 ppm to changes in the oceans carbonate chemistry and coral reef formation.

Here we can also use our model results to some extent to investigate from a modellers perspective, if and how the ocean may have contributed to the observed atmospheric pCO_2 variations. For this we need to keep in mind that the BGC experiments are also forced with observed pCO_2 and don't include coral reefs. Potential mechanisms in our model come from the three 'carbon pumps' of the ocean, i.e. changes of oceanic temperature and circulation (physical pump), alkalinity (alkalinity counter pump), and export production (biological pump).

The simulated export production, the driver of the biological pump, is at a minimum at the time of minimum atmospheric pCO_2 (7 kyr BP), and as such evolves in a way that its contribution to atmospheric pCO_2 would be opposite to the observed evolution. The SST, a driver of the physical pump together with deep water formation rates, evolves in phase with the observed pCO_2, in response to both the orbital forcing and the CO_2 forcing itself. So there is a potential for the orbitally forced change in SST to drive observed pCO_2, and a further contribution from the carbon-cycle climate feedback from the CO_2-forced fraction of SST change, but that feedback is not included in our model.

The general slowdown of the circulation, however, suggests an opposite trend to the one observed, as more dissolved inorganic carbon (DIC) is stored in the deep ocean. Finally, as a result of reduced calcite export, simulated global mean surface alkalinity increases mainly during the mid-Holocene (6.5 kyr to 5 kyr BP), which would lead to decreasing pCO_2 in surface waters and hence a sink for carbon in the atmosphere. The combined effect of all these processes results in diagnosed atmospheric pCO_2 changes of the observed magnitude and an increase in the late Holocene as observed, but with different timing than observed (Fig. 7).

What can be gained from the transient experimens performed here compared to the earlier time-slice climate model experiments at 9.5 kyr BP, 6 kyr BP, and 0 kyr BP with KCM (Schneider et al., 2010) and and also the biogeochemistry experiments with PISCES (Xu et al., 2015)? One obvious gain from the transient experiments is the more complete time coverage over the Holocene, potentially allowing better comparison with proxies and providing more continuous information. The transient experiments can also be used to determine if the timing of the time-slice experiments is appropriate. For the pysical fields like global mean SST (Fig. 2a) we find that the time-slice experiments fit with the extrema of the transient experiment well. Note that the time-slice experiments in Schneider et al. (2010) were performed with preindustrial pCO_2 (286.4 ppm) and hence neglect the forcing from changing atmospheric pCO_2 that is included here.

For the biogechemical variables, however, the picture is more complex. As the state of the biogeochemistry, but also of AMOC in the early and late Holocene are not much different, time slice experiments of these periods would miss any changes in between. Also the time-slice experiments including a 6 kyr BP simulation do not capture the extrema of the simulated time series of the transient experiments BGC-HOL and BGC-HOLx10. E.g., the integrated primary production and export of detritus have their lowest values at 5 kyr to 4 kyr BP (Fig. 10). In particular, the evolution of the EEP OMZ in the non-accelerated experiment BGC-HOL was not captured in the earlier time slice experiments of Xu et al. (2015), even though they also showed smaller mid-Holocene OMZs caused by changes in the equatorial current system.

Finally, are non-accelerated experiments generally required, or can the same knowledge be obtained from experiments with accelerated astronomical forcing? This has already been investigated for physical models (Varma et al., 2016) where a good agreement for physical variables has been found between accelerated and non-accelerated transient simulations over the Holocene in low latitudes, but deviations were found in high latitudes and the deep ocean. When comparing our results for the accelerated and non-accelerated experiments, we find that also the global mean SST shows some deviations, but it is mainly for the biogeochemical system (that was not included in the Varma et al. (2016) model) that large deviations are simulated. This is not only the case for the globally averaged fields, but also more regional at low latitudes such as for the EEP OMZ.

5 Conclusions

This manuscript demonstrates the necessity of performing transient simulations with non-accelerated astronomical forcing when examining the marine biogeochemistry changes over the Holocene. This holds in particular for changes of the oxygen minimum zone in the Eastern Equatorial Pacific, where a strong expansion of the OMZ is simulated in the non-accelerated experiment that cannot be simulated by the accelerated experiment or time slice experiments. While most of the characteristic variables of the marine carbon cycle, like global atmosphere-ocean CO_2-flux, primary and export production, and global mean surface pH display only modest changes during the Holocene, the EEP OMZ-volume increases by more than 50% from early to late Holocene. While the global mean climate remains fairly stable, some abrupt changes can occur in local regions, like the North Atlantic, with a stronger impact also on the nutrient distribution and marine productivity. These variations, however, have little global impact, as variations in the OMZ in the Atlantic south of the equator remain small. An open question remains in why our and other ocean-atmoshere coupled climate models do not simulate the mid-Holocene climate optimum under astronomical and CO_2 forcing. Hopefully, experiments with full scale earth system models that include the land biosphere and a free carbon cycle, and further SST-based proxy records can resolve this decrepency.

Appendix A Simulated and observed oxygen concentrations

Fig. A.1 shows simulated and observation-based O_2-concentration profiles in the three major oxygen minimum zones (OMZ) in the world ocean. For all areas, the simulated oxygen concentrations at the surface are overestimated due to the cold bias in KCM-simulated SST compared to present day estimates of observed SST (Locarini et al., 2013). The near-surface gradient (upper 200 m) is simulated well in the eastern equatorial Pacific (EEP) and the Arabian Sea (AS), but overestimated in the tropical South Atlantic (SATL). Between 200 m and 1000 m, the observed concentation are matched well in the SATL, and differ not too much in the EEP, whereas the observations are poorly matched in the AS, mainly due to a lack of faster sinking large detritus in this area. In general, all BGC simulations show a tendency for too high O_2 concentrations in the upper water column, and too low concentrations below 1000 m, with the exception of the AS. Overall, the representation of oxygen minimum zones is within the range of large scale global ocean biogeochemistry models, that all have there errors (Cabré et al., 2015).

As the threshold for the definition of an OMZ is not very well defined, we display the OMZ volume for a range of threshold values for observaions and as simulated in Fig. A.2 for a) the global ocean, and b) the EEP. For thresholds up to 70 μmol l^{-1}, the simulated OMZ volume is generally too low for the upper 1000 m, while the best match is at a threshold of 80 μmol l^{-1} for the global ocean, and at 70 μmol l^{-1} for the EEP 0-5000 m range. For higher thresholds, the model simulations overestimate the OMZ volume. The respective OMZ volumes for the WOA data (Garcia et al., 2013) are 42 $\times 10^{14} m^3$ for the EEP, and 4.55 $\times 10^{12} m^3$ for the Atlantic OMZ.

Appendix B Changes in the seasonal cycle

Fig. A.3 demonstrates the increasing amplitude of the seasonal cycle of SST and the decreasing amplitude of the seasonal cycle for the ocean-atmosphere carbon flux during the Holocene. For SST, the annual range increases during the first half of the Holocene from about 0.35 °C to about 0.7 °C at 5 kyr BP and remains at that level for the remainder of the Holocene.

For the ocean-atmosphere carbon flux, the seasonal cycle is almost 2 GtC yr^{-1} in the early Holocene, it becomes continously weaker as the Holocene proceeds and is less than 1 GtC yr^{-1} in the late Holocene. Until 5 kyr BP it is mainly the maximum outgassing that becomes weaker, whereas after 5 kyr BP the maximum uptake decreases and turns into outgassing after 3 kyr BP (note that PISCES has an equilibrium outgassing of around 0.5 GtC a^{-1} that compensates the riverine carbon input).

Acknowledgements. J.S. would like to thank the dearly missed Ernst Maier-Reimer for his countless advice and help over many years, Ernst's perpetual willingness to answer his questions and to discuss scientific issues even beyond office hours. At which time, however, discussions were preferably held not in the office but in more enjoyable surroundings, and strictly had to change subject after the third beer – with a bit of luck to his less known months-long journeys from Germany to India and the Saharan Desert by car. This work would not have been possible without him.

The authors acknowledge support by the German Research Foundation through the Collaborative Research Centre Climate-Biogeochemistry Interactions in the Tropical Ocean (SFB754) and the DFG project "Climate impact on marine plankton dynamics during interglacials" (Grant DFG SCH 762/3-1) and the Excellence Cluster Future Ocean (Grant FO EXC 80/1). We also wish to thank Mojib Latif and Wonsun Park for providing the KCM, and the NEMO/PISCES team for providing their models and general support. Computations were carried out on a NEC-SX-ACE at the computing centre of the Christian-Albrechts-University Kiel, Germany. Finally, the authors wish to acknowledge the use of the Ferret programme for analysis and graphics in this paper. Ferret is a product of NOAA's Pacific Marine Environmental Laboratory.

References

Atwood, A., Wu, E., Frierson, D., Battisti, D., and Sachs, J.: Quantifying Climate Forcings and Feedbacks over the Last Millennium in the CMIP5-PMIP3 Models, Journal of Climate, 29, 1161–1178, doi:10.1175/JCLI-D-15-0063.1, 2016.

Aumont, O., Maier-Reimer, E., Blain, S., and Monfray, P.: An ecosystem model of the global ocean including Fe, Si, P colimitations, Global Biogeochemical Cycles, 17, doi:10.1029/2001GB001745, 2003.

Berger, A.: Long-term variations of daily insolation and Quaternary climatic changes, J. Atmos. Sci., 35, 2362–2367, 1978.

Berger, A. and Loutre, M.: Insolation values for the climate of the last 10 million years, Quaternary Science Reviews, 10, 297 – 317, doi:10.1016/0277-3791(91)90033-Q, http://www.sciencedirect.com/science/article/pii/027737919190033Q, 1991.

Bopp, L., Resplandy, L., Orr, J. C., Doney, S. C., Dunne, J. P., Gehlen, M., Halloran, P., Heinze, C., Ilyina, T., Séférian, R., Tjiputra, J., and Vichi, M.: Multiple stressors of ocean ecosystems in the 21st century: projections with CMIP5 models, Biogeosciences, 10, 6225–6245, doi: 10.5194/bg-10-6225-2013, http://www.biogeosciences.net/10/6225/2013/, 2013.

Braconnot, P., Marzin, C., Grégoire, L., Mosquet, E., and Marti, O.: Monsoon response to changes in Earth's orbital parameters: Comparisons between simulations of the Eemian and of the Holocene, Clim. Past, 4, 281294, doi:10.5194/cp-4-281-2008, 2008.

Braconnot, P., Harrison, S., Kageyama, M., Bartlein, P., Masson-Delmotte, V., Abe-Ouchi, A., Otto-Bliesner, B., and Zhao, Y.: Evaluation of climate models using paleoclimatic data, Nat. Clim. Change, 2, 417–424, doi:10.1038/nclimate1456, 2012.

Brovkin, V., Lorenz, S., Jungclaus, J., Raddatz, T., Timmreck, C., Reick, C., Segschneider, J., and Six, K.: Sensitivity of a coupled climate-carbon cycle model to large volcanic eruptions during the last millennium, Tellus B, 62B, 674–681, 2010.

Cabré, A., Marinov, I., Bernardello, R., and Bianchi, D.: Oxygen minimum zones in the tropical Pacific across CMIP5 models: mean state differences and climate change trends, Biogeosciences, 12, 5429–5454, doi:10.5194/bg-12-5429-2015, https://www.biogeosciences.net/12/5429/2015/, 2015.

Cocco, V., Joos, F., Steinacher, M., Frölicher, T. L., Bopp, L., Dunne, J., Gehlen, M., Heinze, C., Orr, J., Oschlies, A., Schneider, B., Segschneider, J., and Tjiputra, J.: Oxygen and indicators of stress for marine life in multi-model global warming projections, Biogeosciences, 10, 1849–1868, 2013.

Dahl-Jensen, D., Mosegaard, K., Gundestrup, N., Clow, G., Johnsen, S., Hansen, A., and Balling, N.:

Past Temperatures Directly from the Greenland Ice Sheet, Science, 282, 268–271, 1998.

Deutsch, C., Brix, H., Ito, T., Frenzel, H., and Thompson, L.: Climate-forced variability of ocean hypoxia, Science, 333, 336–339, doi:doi:10.1126/science.1202422, 2011.

Elsig, J., Schmitt, J., Leuenberger, D., Schneider, R., Eyer, M., Leuenberger, M., Joos, F., Fischer, H., and Stocker, T.: Stable isotope constraints on Holocene carbon cycle changes from an Antarctic ice core, Nature, 461, 507–510, doi:10.1038/nature08393, 2009.

Emile-Geay, J., Cobb, K. M., Carre, M., Braconnot, P., Leloup, J., Zhou, Y., Harrison, S., Correge, T., McGregor, H., Collins, M., Driscoll, R., Elliot, M., Schneider, B., and Tudhope, A.: Links between tropical Pacific seasonal, interannual and orbital variability during the Holocene, Nature Geoscience, 9, 168–173, doi:10.1038/NGEO2608, 2016.

Fichefet, T. and Morales Maqueda, M.: Sensitivity of a global sea ice model to the treatment of ice thermodynamics and dynamics, J. Geophys. Res., 102, 12,609–12,646, 1997.

Garcia, H. E., Locarnini, R. A., Boyer, T. P., Antonov, J. I., Baranova, O. K., Zweng, M. M., Reagan, J. R., and Johnson, D. R.: World Ocean Atlas 2013, Volume 3: Dissolved Oxygen, Apparent Oxygen Utilization, and Oxygen Saturation. S. Levitus, Ed., A. Mishonov, Technical Ed., NOAA Atlas NESDIS 75, U.S. Government Printing Office, Washington, D.C., 2013.

Gaye, B., Böll, A., Segschneider, J., Burdanowitz, N., Emeis, K.-C., Ramaswamy, V., Lahajnar, N., Lückge, A., and Rixen, T.: Glacial-Interglacial changes and Holocene variations in Arabian Sea denitrification, Biogeosciences Discussions, 2017, 1–41, doi:10.5194/bg-2017-256, https://www.biogeosciences-discuss.net/bg-2017-256/, 2017.

Gehlen, M., Bopp, L., Emprin, N., Aumont, O., Heinze, C., and Ragueneau, O.: Reconciling surface ocean productivity, export fluxes and sediment composition in a global biogeochemical ocean model, Biogeosciences, 3, 521–537, doi:10.5194/bg-3-521-2006, http://www.biogeosciences.net/3/521/2006/, 2006.

Heinze, C., Maier-Reimer, E., and Winn, K.: Glacial pCO_2 reduction by the World Ocean: Experiments with the Hamburg carbon cycle model, Paleoceanogr., 6, 1991.

Indermühle, A., Stocker, T., Joos, F., Fischer, H., Smith, H., Wahlen, M., Deck, B., Mastroianni, D., Tschumi, J., Blunier, T., Meyer, R., and Staufer, B.: Holocene carbon-cycle dynamics based on CO_2 trapped in ice at Taylor Dome, Antarctica, Nature, 398, 121–126, 1999.

Jin, L., Schneider, B., Park, W., Latif, M., and Khon, V.: The spatial-temporal pattern of Asian summer monsoon precipitation in response to Holocene insolation change: a model-data synthesis, Quat. Sci. Rev., 85, 47–62, 2014.

Jungclaus, J. H., Lorenz, S. J., Timmreck, C., Reick, C. H., Brovkin, V., Six, K., Segschneider, J., Giorgetta, M. A., Crowley, T. J., Pongratz, J., Krivova, N. A., Vieira, L. E., Solanki, S. K., Klocke, D., Botzet, M., Esch, M., Gayler, V., Haak, H., Raddatz, T. J., Roeckner, E., Schnur, R., Widmann, H., Claussen, M., Stevens, B., and Marotzke, J.: Climate and carbon-cycle variability over the last millennium, Climate of the Past, 6, 723–737, doi:10.5194/cp-6-723-2010, https://www.clim-past.net/6/723/2010/, 2010.

Karstensen, J., Stramma, L., and Visbeck, M.: Oxygen minimum zones in the eastern tropical Atlantic and Pacific Oceans, Progress in Oceanography, 77, 331–350, 2008.

Khon, V. C., Park, W., Latif, M., Mokhov, I. I., and Schneider, B.: Response of the hydrological cycle to orbital and greenhouse gas forcing, Geophysical Reserach Letters, 37, doi:10.1029/2010GL044377, 2010.

Khon, V. C., Park, W., Latif, M., Mokhov, I. I., and Schneider, B.: Tropical circulation and hydrological cycle response to orbital forcing, Geophysical Research Letters, 39, doi:10.1029/2012GL052482, http://dx.doi.org/10.1029/2012GL052482, 2012.

Laskar, J., Robutel, P., Joutel, F., Gastineau, M., Correia, A. C. M., and Levrard, B.: A long-term numerical solution for the insolation quantities of the Earth, Astronomy and Astrophysics, 428, 261–285, doi:10.1051/0004-6361:20041335, 2004.

Leduc, G., Schneider, R., Kim, J. H., and Lohmann, G.: Holocene and Eemian sea surface temperature trends as revealed by alkenone and Ma/Ca paleothermometry, Quat. Sci. Rev., 29, 989–1004, doi:10.1016/j.quascirev.2010.01.1004, 2010.

Lehner, F., Joos, F., Raible, C., Mignot, J., Born, A., Keller, K., and Stocker, T.: Climate and carbon cycle dynamics in a CESM simulation from 850 to 2100 CE, Earth Syst. Dynam., 6, 411–434, doi:10.5194/esd-6-411-2015, 2015.

Locarini, R., Mishonov, A. V., Antonov, J., Boyer, T., Garcia, H., Baranova, O., Zweng, M., Paver, C., Reagan, J., Johnson, D., Hamilton, M., and Seidov, D.: World Ocean Atlas 2013, Volume 1: Temperature. S. Levitus, Ed., A. Mishonov, Technical Ed., NOAA Atlas NESDIS 73, 2013.

Lorenz, S. J. and Lohmann, G.: Acceleration technique for Milankovitch type forcing in a coupled atmosphere-ocean circulation model: method and application for the Holocene, Clim. Dynam., 23, 727743, 2004.

Madec, G.: NEMO ocean engine, Note du Pôle de Modélisation 27, Inst. Pierre - Simon Laplace, Paris, 2008.

Maier-Reimer, E.: Geochemical cycles in an ocean general circulation model: Preindustrial tracer distributions, Global Biogeochem. Cycles, 7, 645–677, 1993.

Maier-Reimer, E. and Hasselmann, K.: Transport and storage of CO_2 in the ocean - An inorganic ocean-circulation carbon cycle model, Clim. Dyn., 2, 63–90, 1987.

Maier-Reimer, E., Mikolajewicz, U., and Hasselmann, K.: Mean Circulation of the Hamburg LSG OGCM and its Sensitivity to the Thermohaline Surface Forcing, J. Phys. Oceanogr., 23, 731–757, 1993.

Maier-Reimer, E., Mikolajewicz, U., and Winguth, A.: Future ocean uptake of CO_2: Interaction between ocean circulation and biology, Clim. Dyn., 12, 711–721, 1996.

Maier-Reimer, E., Kriest, I., Segschneider, J., and Wetzel, P.: The HAMburg Ocean Carbon Cycle model HAMOCC5.1 - Technical description Release 1.1, Reports on Earth System Science 14, Max Planck Institute for Meteorology, 2005.

Marchal, O., Cacho, I., Stocker, T. F., Grimalt, J. O., Calvo, E., Martrat, B., Shackleton, N., Vautravers, M., Cortijo, E., van Kreveld, S., Andersson, C., Ko, N., Chapman, M., Sbaffi, L., Duplessy, J.-C., Sarnthein, M., Turon, J.-L., Duprat, J., and Jansen, E.: Apparent long-term cooling of the sea surface in the northeast Atlantic and Mediterranean during the Holocene, Quaternary Science Reviews, 21, 455 – 483, doi:https://doi.org/10.1016/S0277-3791(01)00105-6, http://www.sciencedirect.com/science/article/pii/S0277379101001056, 2002.

Marcott, S., Shakun, J. D., Clark, P., and Mix, A.: A reconstruction of regional and global temperature for the past 11,300 years, Science, 339, 1189, doi:10.1126/science.1228026, 2013.

Martin, J. H., Knauer, G. A., Karl, D. M., and Broenkow, W. W.: VERTEX: carbon cycling in the northeast Pacific, Deep-Sea Research, 34, 267–286, 1987.

Matear, R. J. and Hirst, C.: Long-term changes in dissolved oxygen concentrations in the ocean caused by protracted global warming, Global Biogeochem. Cycles, 17, 1125, doi:10.1029/2002GB001997, 2003.

Moffitt, S. E., Moffitt, R. A., Sauthoff, W., Davis, C. V., Hewett, K., and Hill, T. M.: Paleoceanographic Insights on Recent Oxygen Minimum Zone Expansion: Lessons for Modern Oceanography, PLoS ONE, 10, e0115 246, doi:10.1371/journal.pone.0115246, 2015.

PAGES 2k Consortium: Continental-scale temperature variability during the past two millennia, Nature Geoscience, 6, 339–346, doi:10.1038/ngeo1797, 2013.

Park, W. and Latif, M.: Multidecadal and Multicentennial Variability of the Meridional Overturning Circulation, Geophysical Research Letters, 35, L22 073, doi:10.1029/2008GL035779, 2008.

Park, W., Keenlyside, N., Latif, M., Ströh, A., Redler, R., Roeckner, E., and Madec, G.: Tropical Pacific Climate and its Response to Global Warming in the Kiel Climate Model, J. Climate, 22, 7192, doi:10.1175/2008JCLI2261.1, 2009.

Renssen, H., Goosse, H., and Fichefet, T.: Contrasting trends in North Atlantic deep-water formation in the Labrador Sea and Nordic Seas during the Holocene, Geophysical Research Letters, 32, L08711, doi:10.1029/2005GL022462, http://dx.doi.org/10.1029/2005GL022462, 2005.

Renssen, H., Seppä, H., Heiri, O., Roche, D., H., G., and Fichefet, T.: The spatial and temporal complexity of the Holocene thermal maximum, Nature Geoscience, 2, 411–414, doi:10.1038/ngeo513, 2009.

Roeckner, E., Bäuml, G., Bonaventura, L., Brokopf, R., Esch, M., Giorgetta, M., Hagemann, S., Kirchner, I., Kornblueh, L., Manzini, E., Rhodin, A., Schlese, U., Schulzweida, U., and Tompkins, A.: The atmospheric general circulation model ECHAM5. Part I: Model description, Report 349, Max Planck Inst. for Meteorol., Hamburg, Germany, 2003.

Salau, O. R., Schneider, B., Park, W., Khon, V., and Latif, M.: Modeling the ENSO impact of orbitally induced mean state climate changes, Journal of Geophysical Research: Oceans, 117, doi:10.1029/2011JC007742, http://dx.doi.org/10.1029/2011JC007742, 2012.

Schmidtko, S., Stramma, L., and Visbeck, M.: Decline in global oceanic oxygen content during the past five decades, Nature, 542, 335–339, doi:10.1038/nature21399, 2017.

Schmittner, A., Galbraith, E., Hostetler, S., Pedersen, T., and Zhang, R.: Large fluctuations of dissolved oxygen in the Indian and Pacific ocean during Dansgaard-Oeschger oscillations caused by variations of North Atlantic Deep Water subduction, Paleoceanography, 22, PA3207, doi:10.1029/2006PA001384, 2007.

Schneider, B., Leduc, G., and Park, W.: Disentangling seasonal signals in Holocene climate trends by satellite-model-proxy integration, Paleoceanography, 25, PA4217, doi:10.1029/2009PA001893, 2010.

Six, K. and Maier-Reimer, E.: Effects of plankton dynamics on seasonal carbon fluxes in a ocean general circulation model, Global Biogeochem. Cycles, 10, 559–583, 1996.

Stramma, L., Johnson, G. C., Sprintall, J., and Mohrholz, V.: Expanding oxygen minimum zones in the tropical oceans, Science, 320, 655–685, 2008.

Takahashi, T., Sutherland, S. C., Chipman, D. W., Goddard, J. G., Newberger, T., and Sweeney, C.: Climatological Distributions of pH, pCO_2, Total CO_2, Alkalinity, and $CaCO_3$ Saturation in the Global Surface Ocean, Ornl/cdiac - 160, ndp - 094, Carbon Dioxide Information Analysis Center, Oak Ridge National Laboratory, U.S. Department of Energy, Oak Ridge, Tennessee, doi:10.3334/CDIAC/OTG.NDP094, 2014.

Varma, V., Prange, M., Merkel, U., Kleinen, T., Lohmann, G., Pfeiffer, M., Renssen, H., Wagner, A., Wagner, S., and Schulz, M.: Holocene evolution of the Southern Hemisphere westerly winds in transient simulations with global climate models, Clim. Past, 8, 391402, doi:10.5194/cp-8-391-2012, 2012.

Varma, V., Prange, M., and Schulz, M.: Transient simulations of the present and the last interglacial climate using the Community Climate System Model version 3: effects of orbital acceleration, Geoscientific Model Development, 9, 3859–3873, doi:10.5194/gmd-9-3859-2016, https://www.geosci-model-dev.net/9/3859/2016/, 2016.

Wanner, H., Beer, J., Bütikofer, J., Crowley, T. J., Cubasch, U., Flückiger, J., Goosse, H., Grosjean, M., Joos, F., Kaplan, J. O., Küttel, M., Müller, S. A., Prentice, I. C., Solomina, O., Stocker, T. F., Tarasov, P., Wagner, M., and Widmann, M.: Mid- to Late Holocene climate change: an overview, Quaternary Science Reviews, 27, 1791 – 1828, doi:https://doi.org/10.1016/j.quascirev.2008.06.013, http://www.sciencedirect.com/science/article/pii/S0277379108001479, 2008.

Xu, X., Segschneider, J., Schneider, B., Park, W., and Latif, M.: Oxygen minimum zone variations in the tropical Pacific during the Holocene, Geophysical Research Letters, 42, 8530–8537, doi:10.1002/2015GL064680, 2015.

Table 1. Experiment names and characteristics. See also Fig. 1a for the temporal evolution of atmospheric pCO_2. BGC-CTL was run for 8,000 years by repeating the forcing from KCM-CTL four times, only the last 2,000 years are used as control experiment.

Experiment name	Model	(orbital) forcing	pCO_2 [ppm]	model years
KCM-CTL	KCM	9.5 kyr BP	263.77	2,000
KCM-HOLx10	KCM	9.5 kyr BP - 0 kyr BP x10	263.77 -286.2	950
KCM-HOL	KCM	9.5 kyr BP - 0 kyr BP	263.77 -286.2	9,500
BGC-CTL	PISCES	KCM-CTL	263.77	2,000 (8,000)
BGC-HOLx10	PISCES	KCM-HOLx10	263.77 -286.2	950
BGC-HOL	PISCES	KCM-HOL	263.77 -286.2	9,500

Biogeosciences Discuss., https://doi.org/10.5194/bg-2017-554
Manuscript under review for journal Biogeosciences
Discussion started: 4 January 2018

Figures

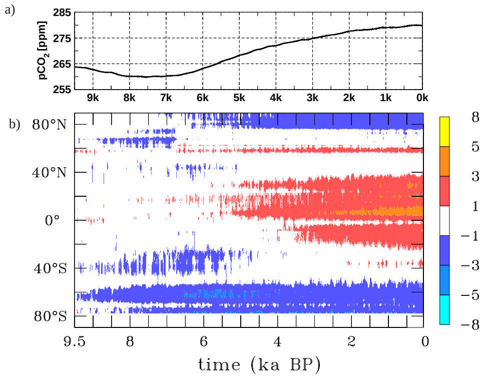

Fig. 1. Forcing for KCM-HOL and BGC-HOL experiments: a) time series of the atmospheric CO_2 concentrations in ppm from Indermühle et al. (1999) and b) short wave radiative forcing at the sea/seaice surface in W m^{-2} for the BGC-HOL experiment as obtained from experiment KCM-HOL (i.e., the astronomical TOA changes over the Holocene as shown in Jin et al. (2014) filterd by ECHAM5, the atmospheric component of KCM). Hovmöller diagramme of the anomaly of zonal and annual mean for the last 9,500 years as 50 year running mean. Anomalies are derived by subtracting the average over the first 200 years from the annual mean values.

Biogeosciences Discuss., https://doi.org/10.5194/bg-2017-554
Manuscript under review for journal Biogeosciences
Discussion started: 4 January 2018

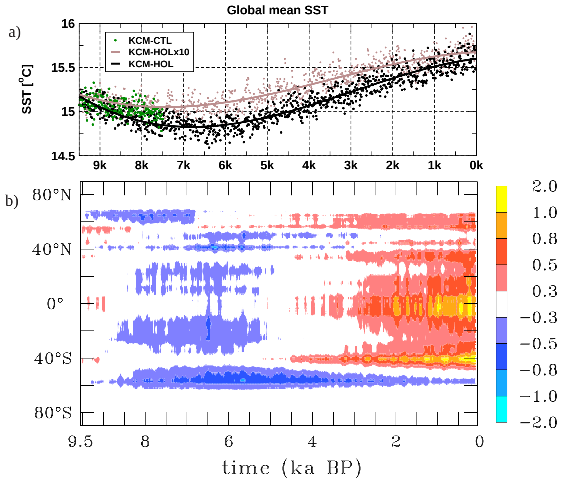

Fig. 2. a) time series of annual and global mean SST in °C for the three KCM experiments KCM-HOL (non-accelerated forcing, black), KCM-HOLx10 (10 times accelerated forcing, brown), and the control experiment KCM-CTL (green dots). Circles represent annual averages (not every year shown), solid lines a 4th order polynomial fit. b) Hovmöller diagramme of the zonmal mean SST anomaly in °C for KCM-HOL, computed by subtracting the average over the first 20 years of KCM-HOL from annual mean values and smoothed by a 10 yr running mean. See colour bar for contour intervals.

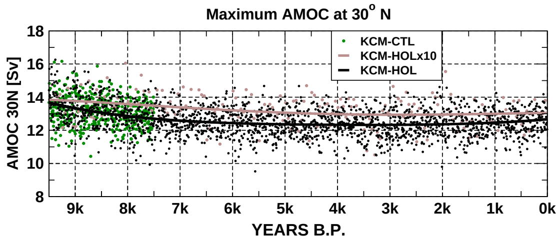

Fig. 3. As in Fig. 2a, but for the maximum meridional overturning in the Atlantic at 30 °N in Sv (10^6 m^3 s^{-1}).

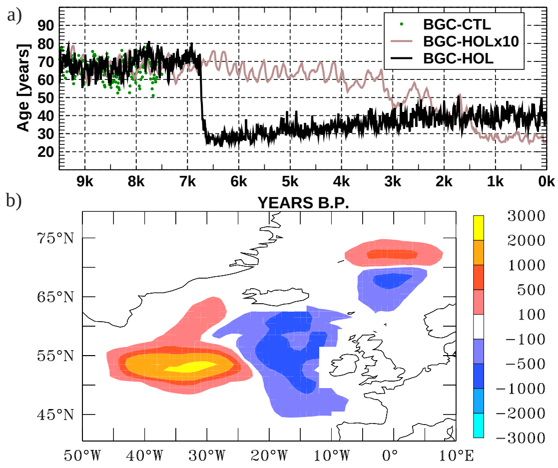

Fig. 4. a) Idealized age (time since contact with the surface,in years) averaged over a volume in the deep North Atlantic (40°W - 10°W, 40°N - 60°N, 1800 m - 2500 m depth) based on annual mean values for KCM-HOL (black), KCM-HOLx10 (brown) and KCM-CTL (green dots). b) Change in annual maximum mixed layer depth in m in the North Atlantic between two periods before and after the shift in watermass age (5.8 minus 7.8 kyr BP, mean over 200 years centred around the respective dates), indicating a shift in the location and the intensity of deep water formation.

Biogeosciences Discuss., https://doi.org/10.5194/bg-2017-554
Manuscript under review for journal Biogeosciences
Discussion started: 4 January 2018

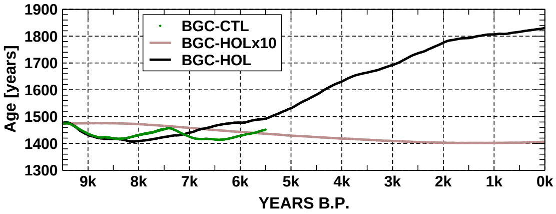

Fig. 5. As Fig. 4a, but for the idealized age in years averaged over a volume in the deep North Pacific (150°E - 130°W, 40°N -60°N, 2500 m - 3500 m depth) and BGC-CTL extended for another 2000 years to make sure that the increase in age after 8.5 kyr BP is not continuing as in BGC-HOL.

Biogeosciences Discuss., https://doi.org/10.5194/bg-2017-554
Manuscript under review for journal Biogeosciences
Discussion started: 4 January 2018

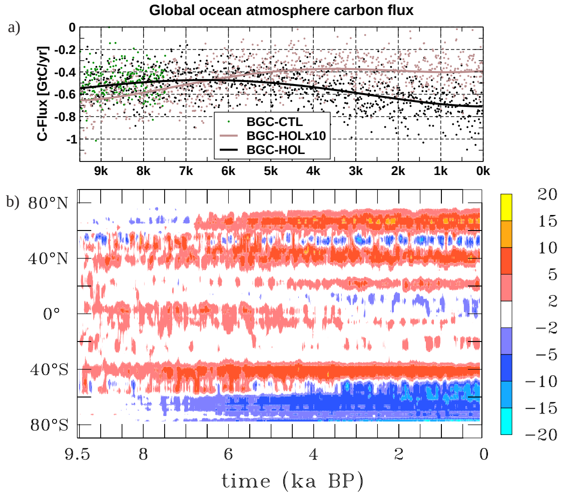

Fig. 6. As Fig. 2, but a) for the global atmosphere-ocean carbon flux (GtC yr^{-1}) of experiments BGC-HOL (black), BGC-HOLx10 (brown) and BGC-CTL (green). Negative values indicate oceanic outgassing. The net outgassing of around 0.5 GtC yr^{-1} is balancing the river input of carbon. b) Hovmöller diagramme of the zonal mean atmosphere-ocean carbon flux change (mol C m^{-2} s^{-1}) of experiment BGC-HOL. Positive anomalies indicate stronger uptake at latitudes of net CO$_2$-flux into the ocean, or weaker outgassing in areas of a net CO$_2$-flux into the atmosphere (60°S to 45°S and 20°S to 17°N). Negative values vice versa. The negative anomaly in the high southern latitudes indicates a shift from net uptake to net outgassing.

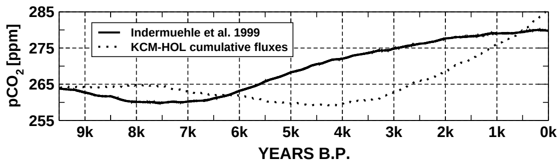

Fig. 7. Observed atmospheric pCO$_2$ (solid, as in Fig.1a) that is used to force experiment BGC-HOL, together with the potential atmospheric pCO$_2$ derived from the time integrated ocean to atmosphere fluxes in experiment KCM-HOL (dotted) where pCO$_2$(t)=pCO$_2$(t-1)+ 0.5 * CO$_2$-flux(t) and the CO$_2$-flux is the global sum in GtC/month and pCO$_2$($_{9.5kyrBP}$)=263.77ppm.

Biogeosciences Discuss., https://doi.org/10.5194/bg-2017-554
Manuscript under review for journal Biogeosciences
Discussion started: 4 January 2018

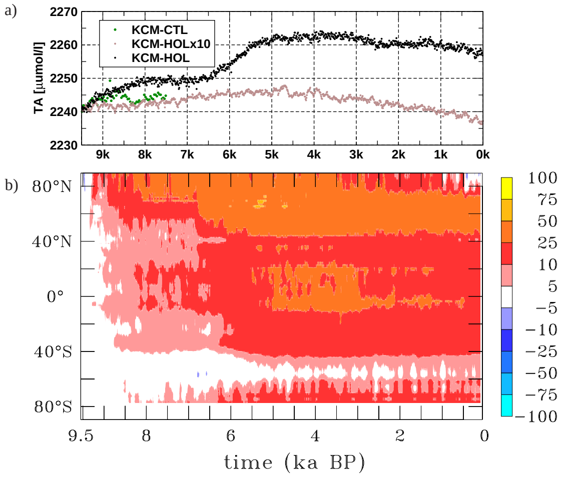

Fig. 8. As Fig. 2, but for a) time series of global mean total alkalinity (TA) at the surface in μmol l^{-1} where dots represent annual mean values, and b) Hovmöller diagramme of the changes in zonal mean annual mean surface TA in μmol l^{-1}.

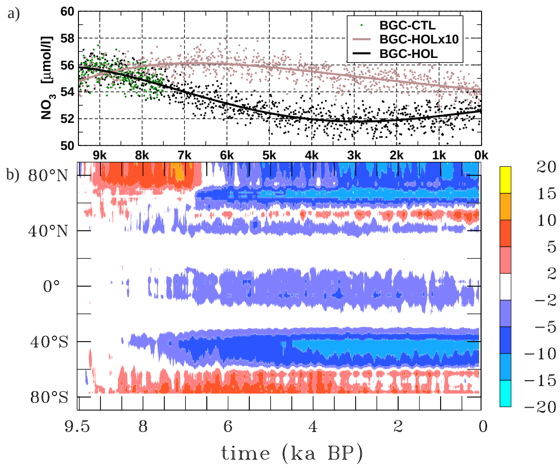

Fig. 9. As Fig. 2, but a) for the NO_3 concentration averaged over the uppermost 100 m in μmol l^{-1} and b) Hovmöller diagramme of the changes in zonal and annual mean NO_3 concentration in the upper 100 m in μmol l^{-1}.

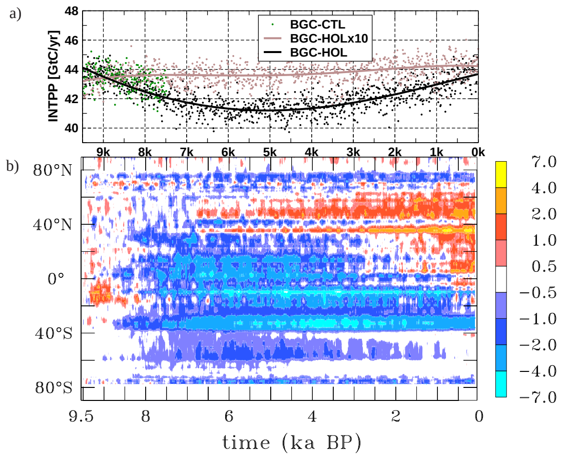

Fig. 10. As Fig. 2, but a) for time series of global primary production integrated over the upper 100 m (INTPP) in GtC yr^{-1} and b) Hovmöller diagramme of the changes in INTPP in mol $\mathrm{m}^{-2}\ \mathrm{s}^{-1}$ x 10^{-8}.

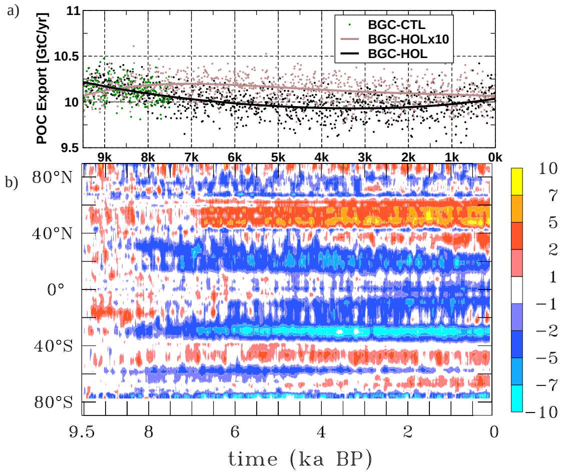

Fig. 11. As Fig. 2, but a) for time series of global export production at the bottom of the euphotic layer in GtC yr^{-1} and b) Hovmöller diagramme of the changes in global export production in mol m^{-2} s^{-1} x 10^{-9}.

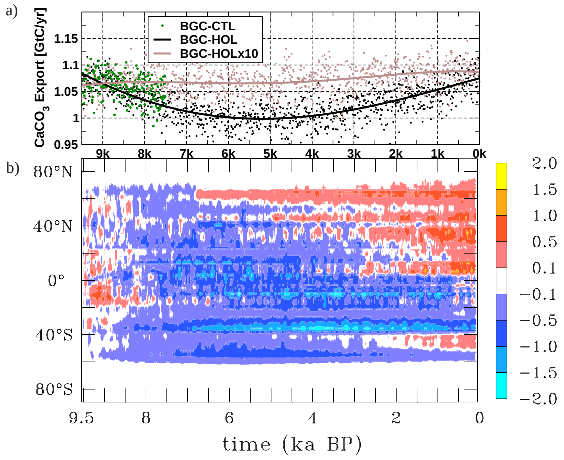

Fig. 12. As Fig. 2, but a) for time series of global $CaCO_3$ export production at the bottom of the euphotic layer in GtC yr^{-1} and b) Hovmöller diagramme of change in $CaCO_3$ export in mol C m^{-2} s^{-1} x 10^{-9}.

Biogeosciences Discuss., https://doi.org/10.5194/bg-2017-554
Manuscript under review for journal Biogeosciences
Discussion started: 4 January 2018

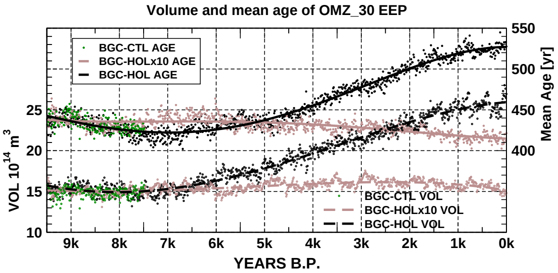

Fig. 13. Time series of Eastern Equatorial Pacific OMZ volume in 10^{14} m^3 (lower curves, left scale) and mean age of water mass (upper curves, right scale) in the EEP OMZ in years in the area 140°W - 74°W, 10°S - 10°N. Circles represent annual mean values of the OMZ volume, dots are annual mean values of the water mass age in the EEP OMZ for BGC-HOL (black), BGC-HOLx10 (brown) and BGC-CTL (green). Solid (age) and dashed (volume) lines represent polynomial fits of 4th order.

Biogeosciences Discuss., https://doi.org/10.5194/bg-2017-554
Manuscript under review for journal Biogeosciences
Discussion started: 4 January 2018

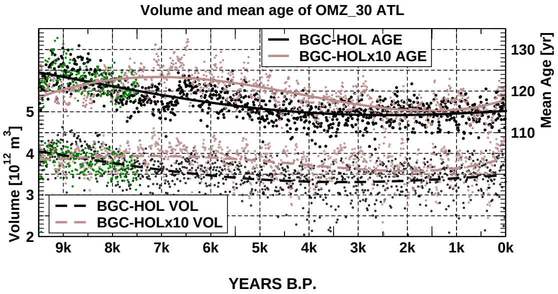

Fig. 14. As Fig. 13 but for the Atlantic in the area of 5°W - 15°E, 30°S - 5°N and OMZ volume in 10^{12} m^3.

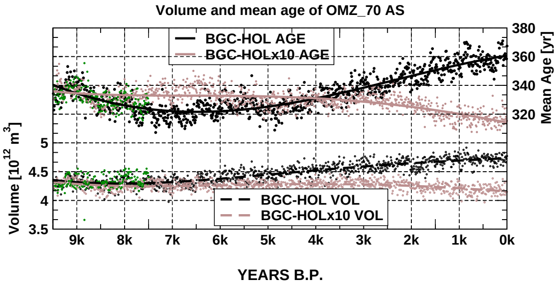

Fig. 15. As Fig. 13 but for the Arabian Sea in the area of 55°E - 75°E, 8.5°N - 28°N and OMZ volume in 10^{12} m^3.

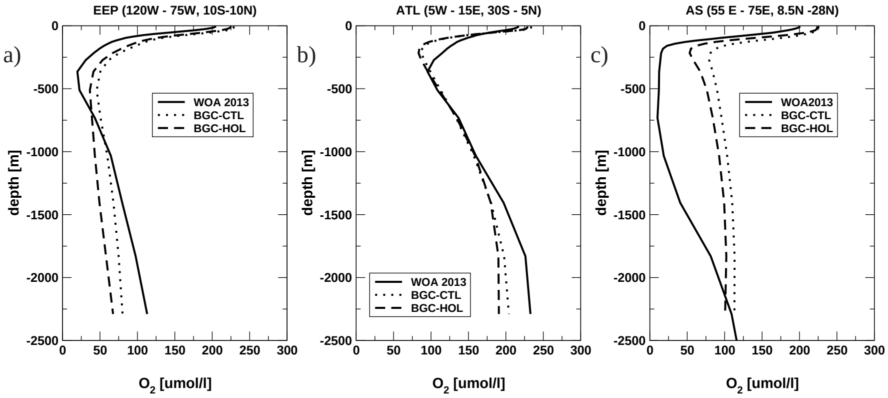

Fig. A.1. Simulated and observation based profiles of average O_2-concentration in the three major oxygen minimum zones in the world ocean for a) the eastern equatorial Pacific, b) the tropical South Atlantic, and c) the Arabian Sea based on observations (WOA2013, Garcia et al. (2013), solid), and from experiments BGC-CTL (dotted) and averaged over the last 200 years of BGC-HOL (dashed).

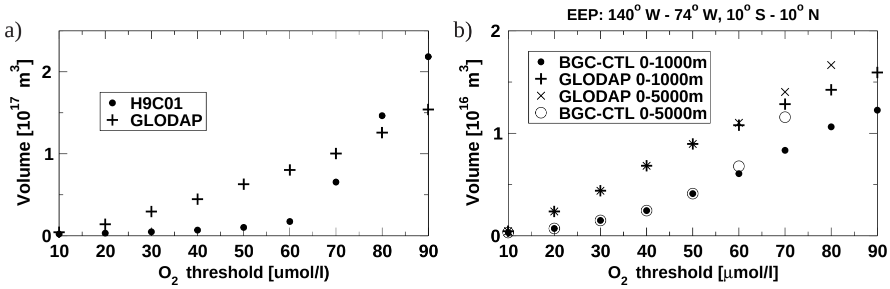

Fig. A.2. Simulated and observation based volume of water masses with oxygen concentration below the threshold value indicated on the x-axis for a) the world ocean and b) the eastern equatorial Pacific. See legends for explanations of symbols.

Biogeosciences Discuss., https://doi.org/10.5194/bg-2017-554
Manuscript under review for journal Biogeosciences
Discussion started: 4 January 2018

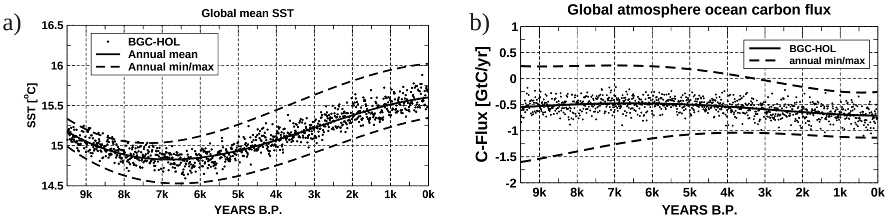

Fig. A.3. Time series of ocean atmosphere carbon flux (negative upward) for experiment BGC-HOL (black dots: annual mean values, solid black line: 4th order polynomial fit), and annual minimum and maximum (dashed black lines, 4th order polynomial fits), indicating the range of the annual cycle.